Journal of Power Sources 242 (2013) 472–477

Contents lists available at SciVerse ScienceDirect

Journal of Power Sources

journal homepage: www.elsevier.com/locate/jpowsour

Nanofluidic fuel cell

Jin Wook Lee, Erik Kjeang*

School of Mechatronic Systems Engineering, Simon Fraser University, 250-13450 102 Avenue, Surrey, BC V3T 0A3, Canada

HIGHLIGHTS

- For the first time, the concept of nanofluidics is utilized in a fuel cell.
- The proposed nanofluidic fuel cell is membraneless and catalyst-free.
- The nanoporous electrodes show superior electrochemical kinetics.
- The fuel cell performance is enhanced in the high cell voltage regime.

GRAPHICAL ABSTRACT

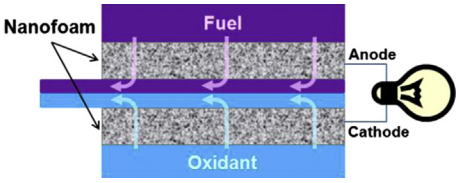

ARTICLE INFO

Article history:
Received 11 March 2013
Received in revised form
16 May 2013
Accepted 23 May 2013
Available online 5 June 2013

Keywords:
Fuel cell
Nanofluidic
Microfluidic
Membraneless
Nanofoam
Nanotechnology

ABSTRACT

Fuel cells are gaining momentum as a critical component in the renewable energy mix for stationary, transportation, and portable power applications. State-of-the-art fuel cell technology benefits greatly from nanotechnology applied to nanostructured membranes, catalysts, and electrodes. However, the potential of utilizing nanofluidics for fuel cells has not yet been explored, despite the significant opportunity of harnessing rapid nanoscale reactant transport in close proximity to the reactive sites. In the present article, a nanofluidic fuel cell that utilizes fluid flow through nanoporous media is conceptualized and demonstrated for the first time. This transformative concept captures the advantages of recently developed membraneless and catalyst-free fuel cell architectures paired with the enhanced interfacial contact area enabled by nanofluidics. When compared to previously reported microfluidic fuel cells, the prototype nanofluidic fuel cell demonstrates increased surface area, reduced activation overpotential, superior kinetic characteristics, and moderately enhanced fuel cell performance in the high cell voltage regime with up to 14% higher power density. However, the expected mass transport benefits in the high current density regime were constrained by high ohmic cell resistance, which could likely be resolved through future optimization studies.

1. Introduction

Laminar flow based fuel cells (LFFCs) [1], also known as membraneless or microfluidic fuel cells [2], is a recently developed fuel cell technology that operates using microscale co-laminar parallel streaming of fuel and oxidant electrolytes in place of an ion-conducting membrane in the space between the two electrodes (anode and cathode). In contrast to conventional hydrogen and methanol fuel cells comprising a membrane electrode assembly design in a layered sandwich configuration, membraneless fuel cells can be fabricated in a unibody design that benefits from compatibility with standard micromachining and MEMS fabrication methods [3]. Moreover, the cost and durability issues associated with ion-conducting membranes are eliminated [4]. A variety of microfluidic fuel cell devices operating on liquid and gaseous fuels and oxidants have been demonstrated to date [4,5]with typical microchannel cross-sectional dimensions between 10 μm and 1 mm. In terms of dimensions, the upper bound is not only formally restricted by the definition of 'microfluidics' but also fundamentally by the hydrodynamics that ultimately transitions into turbulent flow at high Reynolds numbers and disrupts the co-laminar streaming. The lower bound, in contrast, has no fundamental limit

* Corresponding author. Tel.: +1 778 782 8791; fax: +1 778 782 7514.
E-mail address: ekjeang@sfu.ca (E. Kjeang).

0378-7753/$ – see front matter © 2013 Elsevier B.V. All rights reserved.
http://dx.doi.org/10.1016/j.jpowsour.2013.05.129

other than the constraints imposed by fabrication. It is well-established, however, that the surface-area-to-volume ratio of microchannels scale as the inverse of the length scale [2], and thereby increases proportionally with decreasing size. Fuel cells, having surface-based electrochemical reactions, would consequently stand to benefit from further miniaturization.

Nanomaterials as electrodes and electrolytes in energy conversion and storage devices such as lithium ion batteries, fuel cells, and supercapacitors were investigated by various researchers [6]. For fuel cell applications, a promising concept based on an array of nanochannels as proton conductive membrane was investigated by Liu et al. [7]. Due to the electric double layer overlap enabled by the nanochannels, the proton conductivity was enhanced by orders of magnitude with improved fuel cell performance. Moghaddam et al. [8] demonstrated a silicon-based inorganic–organic membrane with 5–7 nm pores for a similar purpose. A scalable nanostructured membrane for solid oxide fuel cells was reported by Tsuchiya et al. [9]: nanoscale yttria-stabilized zirconia membranes were combined with a nanostructured dense oxide cathode in a thin-film architecture to increase the performance of these cells. On the contrary, no published studies have explored the opportunity of utilizing nanomaterials for membraneless fuel cells, nor has the concept of nanofluidics been previously applied to fuel cells. The practical use of nanoscale channels or pores in membraneless fuel cells is however dependent on the timescale for interdiffusive mixing between the two co-laminar streams. The mixing timescale is proportional to the channel width and governed by the Péclet number for mass diffusion, given by $Pe = LU/D$, where L is the characteristic length for diffusion, U the mean velocity, and D the mass diffusion coefficient. The mixing timescale in nanochannels is therefore three orders of magnitude faster than in previously employed microchannels [10], and must be taken into account for practical design of nanofluidic fuel cells.

The objective of the present work is to develop and demonstrate a membraneless nanofluidic fuel cell architecture that captures the combined advantages of reactant flow on the nanoscale and high surface area electrodes. The proposed fuel cell features flow through nanoscale conduits in an electrochemically active and conductive nanoporous media. The mixing constraint described above is mitigated in this case by utilizing a central microchannel with sufficiently large dimensions intended to delay the mixing of fuel and oxidant, as previously demonstrated by our group [11]. The proposed fuel cell is thereby capable of exploiting high nanoscale transport rates *inside* the electrodes without compromising the stability of the co-laminar flow in the space *between* the electrodes.

2. Methodology

2.1. Fuel cell design

In the proposed nanofluidic fuel cell, a conductive nanoporous electrode material is incorporated with a membraneless, miniaturized fuel cell architecture, as shown in Fig. 1. The overall device layout features a flow through porous electrode design [12]. Fuel and oxidant are supplied by a syringe pump via separate inlet ports and forced to flow through the internal nanoscale pores of the nanoporous electrodes on the anode and cathode sides, respectively. In the microfluidic channel at the center of the device, the two opposite streams exiting the nanoporous media are forced to make a 90° turn and flow in a co-laminar format on the microscale toward an orthogonally situated outlet. The 'nanofluidic fuel cell' terminology used in this work refers to the *nanofluidic* flow inside the nanoporous electrodes, where the electrochemical reactions take place, while the flow in the center channel is *microfluidic* due to the microscale dimensions of the channel. The present device is

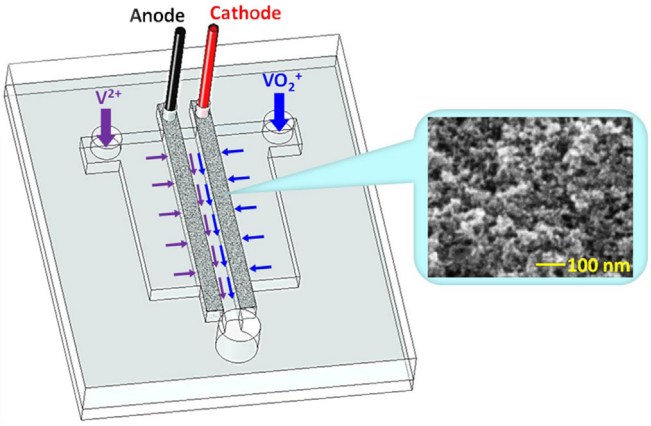

Fig. 1. Schematic of the nanofluidic fuel cell employing carbon nanofoam electrodes in a membraneless, catalyst-free configuration. The liquid fuel (V^{2+}) and oxidant (VO_2^+) flow orthogonally through the nanoporous electrodes and exit into the central channel, where a parallel, co-laminar flow is established toward the downstream outlet.

generally categorized as a microfluidic electrochemical cell but described here as a *fuel cell* [1–5], provided its main function of electrochemical power generation from continuously supplied fuel and oxidant. Notably, the device also meets the definition of a primary redox flow battery for discharge operation. However, the present single-outlet design is not suitable for regenerative operation; certain device-level modifications are required to facilitate operation as a rechargeable, secondary redox flow battery, as described elsewhere [13].

Vanadium redox electrolyte, which has become the industry standard for grid-scale vanadium redox batteries [14], is employed as fuel (V^{2+}, denoted as V(II)) and oxidant (VO_2^+, denoted as V(V)) in the present study to benchmark the performance of the nanofluidic fuel cell in relation to existing microfluidic fuel cell devices with carbon paper electrodes [12,15]. The cell operation is based on the following anodic and cathodic reactions at room temperature [16]:

$$V^{3+} + e^- \rightleftarrows V^{2+} \qquad E^\circ = -0.496\ \text{V vs. SCE} \tag{1}$$

$$VO_2^+ + 2H^+ + e^- \rightleftarrows VO^{2+} + H_2O \qquad E^\circ = 0.750\ \text{V vs. SCE} \tag{2}$$

The theoretical standard cell potential is 1.246 V but this can, however, be increased up to 1.5 V depending on the concentration ratio of the vanadium species. Provided that the vanadium redox reactions are rapid on carbon, the present fuel cell device is not only membraneless but also catalyst-free. As previously reported [12], 2 M vanadium redox electrolyte solutions in 4 M sulfuric acid are prepared from stock electrolyte. The active species concentrations (V(V) and V(II)) used in this work are 92% (equivalent to 1.84 M) or higher and all measurements are recorded at room temperature.

2.2. Electrode material

A conductive nanoporous material based on carbon aerogels is investigated and employed as the main electrode material. Developed at Lawrence Livermore National Laboratory [17], carbon aerogels are synthesized by the sol–gel polycondensation of resorcinol and formaldehyde, followed by supercritical drying and pyrolysis in an inert atmosphere. This innovative fabrication process yields unique carbon foams that are characterized by high porosity, high surface area, and ultrafine pore sizes (less than 50 nm) [18,19]. The key advantage of carbon nanofoam as potential electrodes of electrochemical devices over conventional carbon papers is its high

surface area of 400–800 $m^2\ g^{-1}$ [20,21], which is approximately 2000× higher than the carbon paper having a mass specific area of $190 \times 10^{-3}\ m^2\ g^{-1}$ [11]. Carbon nanofoam can also be fabricated by infiltrating carbon paper with phenolic resin to create electrically conductive sheets of ultraporous carbon structure[22].

In the current work, the carbon nanofoam material (Type I, measured thickness ~ 180 μm) employed as electrodes in the nanofluidic fuel cell is supplied by MarkeTech International and was originally developed as an alternative electrode material to woven carbon cloth [23]. Fig. 2 shows scanning electron microscope (SEM) images of the nanofoam, featuring (a) top-down and (b) cross-sectional views. Randomly distributed as back-bones providing mechanical stability and high electrical conductivity, carbon fibers are interspersed with the nanoporous filler structure that visually appears as a solid in these images. The true internal nanostructure of the nanofoam is revealed by the high-magnification image provided in Fig. 1, which represents the region indicated by the red box in Fig. 2(b). The characteristic pore sizes are 10–100 nm in diameter. Crack-like surface pores (10–30 μm in diameter), likely originating from manufacturing defects, are also seen in the SEM images. According to the manufacturer's specification, the gas permeability of the nanofoam is on the order of $10^{-10}\ m^2$ [23], which is *higher* than that of the carbon paper [24] and consequently the pressure drop across the nanofoam is expected to be *lower*. The pumping power requirements for the device operation are therefore estimated to be less than 0.1% of the power output [15].

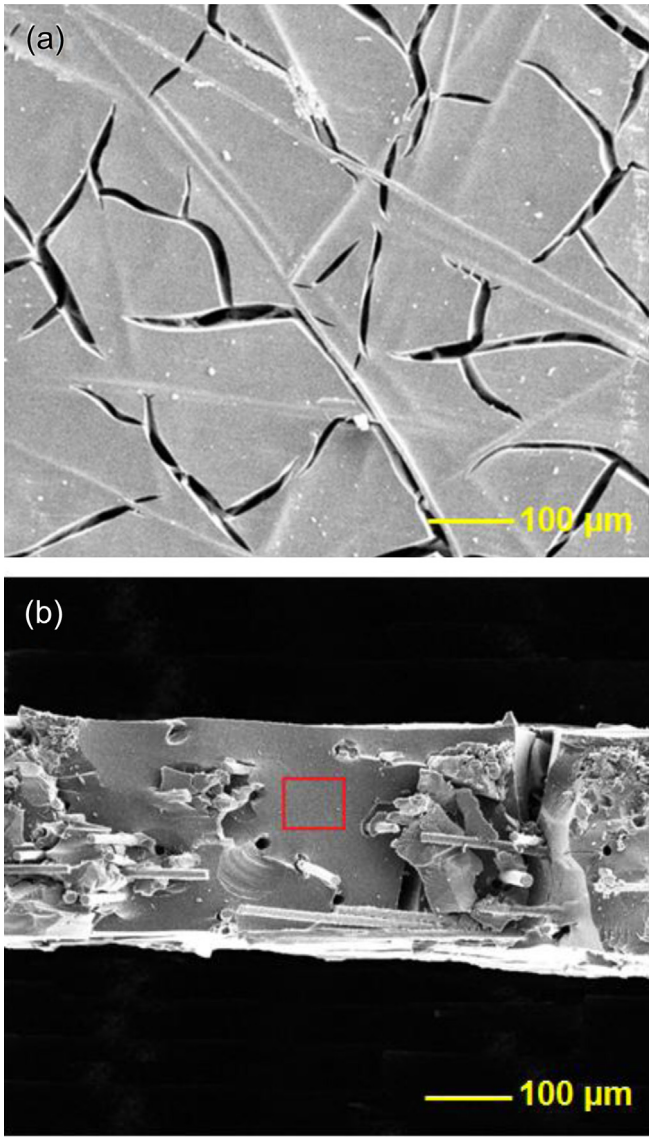

Fig. 2. Scanning electron microscope (SEM) images of the carbon nanofoam used as electrodes in the nanofluidic fuel cell: (a) top view; and (b) cross section.

2.3. Ex situ measurements

Electrochemical *ex situ* measurements of vanadium redox reactions on carbon nanofoam electrodes, including impedance spectroscopy and Tafel analysis, are first conducted to investigate the ohmic and electrochemical properties of the nanofoam material in the context of the present application. A standard three-electrode electrochemical cell controlled and operated by a frequency response analyzer (FRA) capable potentiostat (Reference 3000, Gamry Instruments) is employed [25]. The stationary working electrodes have identical dimensions to the actual electrode prepared for nanofluidic fuel cell integration: 18 mm long, 1 mm wide, and 0.18 mm thick [15]. Further details on the experimental setup and procedure can be found in a previous report [25].

The overall ohmic resistance and resistivity of the nanofoam material are determined *ex situ* by electrochemical impedance spectroscopy (EIS). Impedance spectra are measured in V(V) solution with an AC amplitude of 10 mV rms over the frequency range from 150 kHz to 10 Hz (at OCP ≈ 0.956 V vs. SCE). The net electrode resistance is estimated by subtracting 1 Ω from the high-frequency real-axis intercept in the obtained Nyquist plots, assuming the sum of contact and solution resistances to be approximately 1 Ω. For these experiments, the electrolyte solutions are kept still without agitation to impose a pure diffusion condition. The resistivity values are finally calculated from the obtained data using Ohm's law and the electrode dimensions ($18 \times 1 \times 0.18$ mm).

A linear potential sweep polarization technique is employed to obtain Tafel curves and investigate the electrochemical kinetics of the vanadium redox reactions on the carbon nanofoam material. The current response at the working electrode is measured while the potential between the working and reference electrodes is swept linearly at a low, constant scan rate of 0.1 mV s^{-1}. This linear polarization is performed in the overpotential range of 0 ~ 200 mV (with respect to the open circuit potential) for both V(V) reduction and V(II) oxidation reactions. For these measurements, the electrolytes in the three-electrode electrochemical cell are stirred by a magnetic spinner (Corning, PC-220) to decouple mass transport limit effects as much as possible. The current densities reported in the Tafel plots are calculated based on the submerged geometrical surface area of the electrodes. A simple, single electron transfer reaction is assumed as the rate determining step in the vanadium redox kinetics [26] and the simplified form of the Butler–Volmer equation is adapted for the analysis [27,28]. The exchange current density j_o is calculated from the y-intercept point, followed by estimating the rate constant k_o. To ensure repeatable and consistent data, the measurements are repeated at least three times on different days.

2.4. In situ fuel cell experiments

Prototype nanofluidic fuel cells employing carbon nanofoam as electrodes are fabricated using a standard microfabrication procedure based on soft lithography in polydimethylsiloxane (PDMS) using a master (mold) with measured height of approximately 150 μm to ensure sufficient compression of the nanofoam electrodes. Further details about the fabrication process can be found elsewhere [15]. The fuel, V(II), and oxidant, V(V), solutions are

supplied via two separate inlet ports and flow continuously through the nanofoam electrodes that are glued to external wires with conductive epoxy. Fuel cell polarization curves are measured as described in the previous reports at a flow rate of 10 μL min^{-1} [12,15]. The current densities and power densities reported here are normalized based on the top surface area of each electrode.

3. Results and discussion

Nanofluidic fuel cell prototypes featuring flow through conductive nanoporous electrodes are fabricated, tested, and investigated. The carbon nanofoam employed as electrode material is first analyzed by electrochemical *ex situ* measurements performed in vanadium redox electrolytes. Subsequently, complete fuel cell polarization curves are measured *in situ* for the nanofluidic fuel cell devices with embedded nanofoam electrodes. The overall fuel cell performance is evaluated in the context of the *ex situ* results and compared to existing literature data, and the advantages of the nanofluidic fuel cell concept are discussed.

3.1. Electrochemical ex situ analysis

The overall ohmic resistance and resistivity of the nanofoam material are determined *ex situ* by electrochemical impedance spectroscopy from the high-frequency real-axis intercept. The corresponding resistivity value of the nanofoam determined by Ohm's law and the submerged electrode dimensions is $(2.4 \pm 0.6) \times 10^{-2}$ Ω cm, while the value for regular carbon paper is $(6.1 \pm 0.1) \times 10^{-3}$ Ω cm [25]. The resistivity of the nanofoam electrode is thus approximately 4× higher than that of regular carbon paper and is in good agreement with the manufacturer's specification of $10–40 \times 10^{-3}$ Ω cm.

In order to determine the electrochemical kinetic parameters of the vanadium redox reactions with respect to the nanofoam electrodes, a comprehensive Tafel analysis is conducted. With increased ohmic potential drops due to the high resistivity of nanofoam, *IR* compensation is essential in the Tafel analysis to decouple the kinetic and ohmic overpotentials. Fig. 3 shows the effect of *IR* compensation on V(V) reduction resulting from the overall ohmic resistance of carbon nanofoam. The compensation is found to contribute up to 45 mA cm^{-2}, which causes a significant upward shift in the Tafel plots, and is therefore important for unbiased and accurate estimation of kinetic parameters. The *IR* compensated Tafel plots for the nanofoam material investigated in this study are provided with a comparison to the regular carbon paper in Fig. 4 for (a) V(V) reduction and (b) V(II) oxidation. The main observations from the Tafel plots are summarized as follows:

- Compared to the regular carbon paper [25], the nanofoam electrodes show significantly improved kinetic rates for both V(V) reduction and V(II) oxidation, and the relative degree of enhancement is greater in V(II) oxidation where more than 10× higher current densities are obtained.
- In general, V(V) reduction kinetics are faster than V(II) oxidation on the nanofoam electrodes. These findings are consistent with data obtained for solid glassy carbon electrodes [29–31]. However, the difference in *y*-intercept values between the V(V) and V(II) curves is significantly reduced compared to the carbon paper, which results in more well-balanced kinetic rates between the V(V) and V(II) half-cells.

The rate constants (k_o) estimated from the Tafel curves for both V(V) reduction and V(II) oxidation reactions are listed in Table 1. As mentioned, the kinetic rates obtained on carbon nanofoam electrodes are significantly faster than those of the carbon paper: for V(II) oxidation, the nanofoam shows 9.2× higher rate constant,

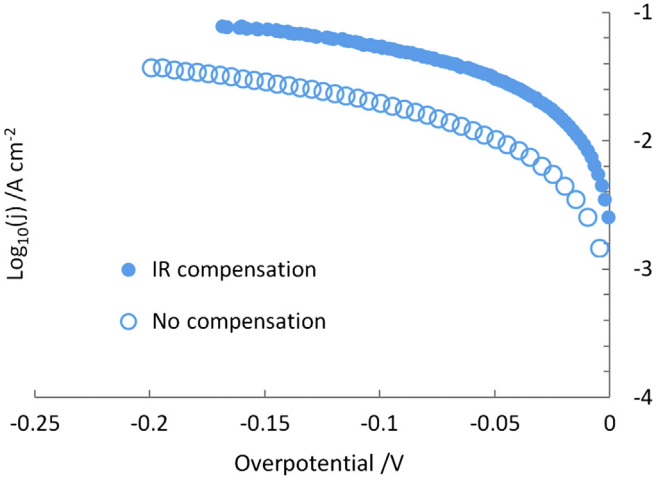

Fig. 3. Effect of *IR* compensation in the Tafel plot for V(V) reduction on the nanofoam electrode.

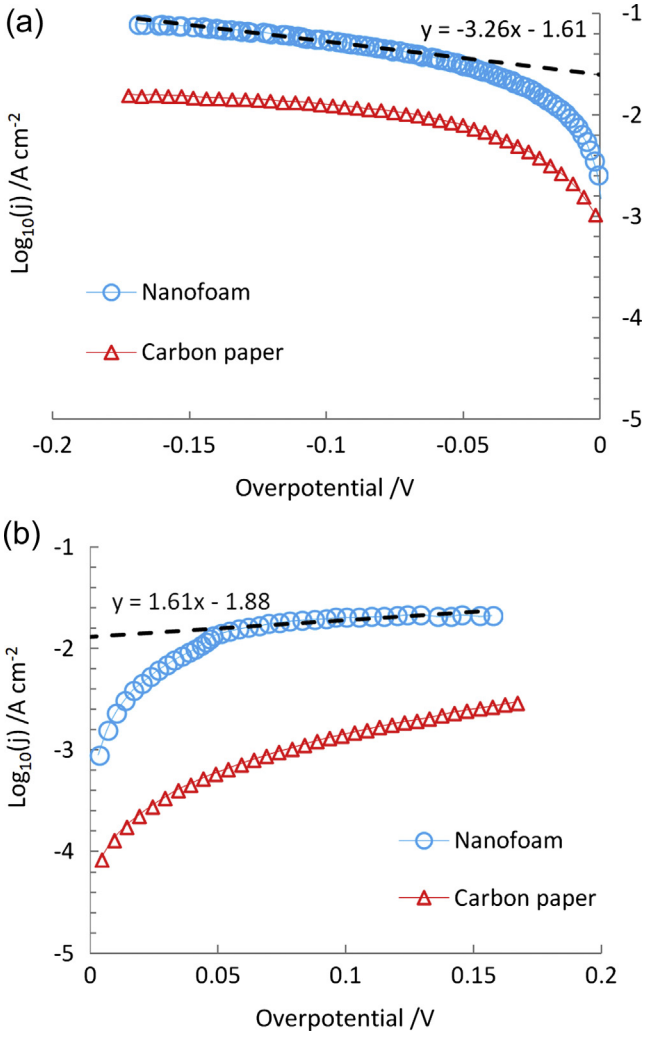

Fig. 4. *IR* compensated Tafel plots measured *ex situ* for (a) V(V) reduction and (b) V(II) oxidation. The linear regression lines for the nanofoam are shown by the dashed lines with corresponding equations.

Table 1
Rate constants (k_o) estimated from Tafel plots.

	k_o for V(V)/cm s^{-1}	k_o for V(II)/cm s^{-1}
Nanofoam	$(3.30 \pm 0.00) \times 10^{-4}$	$(5.10 \pm 0.01) \times 10^{-5}$
Carbon paper [24]	$(6.36 \pm 0.15) \times 10^{-5}$	$(5.54 \pm 0.15) \times 10^{-6}$

while 5.2× higher for V(V) reduction. Consequently, it is anticipated that the activation overpotential for fuel cell operation employing the nanofoam electrodes would be reduced. In addition, the charge transfer coefficient (α) values for both V(V) reduction and V(II) oxidation indicate that the vanadium redox reactions on the nanofoam under present conditions are asymmetric, which is consistent with our previous study of solid graphite and carbon paper electrodes in the same electrolytes [25].

3.2. In situ fuel cell analysis

The prototype nanofluidic fuel cells are tested experimentally and benchmarked against the present state-of-the-art microfluidic fuel cell with regular carbon paper electrodes [15]. Since the electrolytes, supply rate, and central microchannel dimensions are intended to be identical for the two types of fuel cells, the main difference between the cells is attributed by the internal nano/microstructure of the electrode materials, where the nanofoam has three orders of magnitude smaller characteristic pore size than the carbon paper. Fuel cell polarization curves, provided in Fig. 5, are measured *in situ* with each device and compared to examine the fuel cell performance at 10 μL min^{-1} flow rate.

As anticipated from the Tafel analysis, the nanofluidic fuel cell shows significantly lower kinetic or activation overpotentials compared to the microfluidic cell and improved performance at high cell voltages. More specifically, the first three data points of the nanofluidic cell do not have a noticeable drop in cell potential (less than 5 mV), while the initial cell potential drop of the microfluidic cell is clearly seen in Fig. 5(b). It is estimated that the activation losses are reduced by up to 150 mV, although it may be partially masked by other sources of voltage losses. These improvements are equivalent to a 14% increase in cell voltage. In the linear regime where the ohmic overpotentials are dominating, the slope of the nanofluidic cell is however steeper than that of the baseline. This trend is consistent with the impedance measurements: the overall ohmic resistance of the nanofoam is 4× higher than the carbon paper, which constrains the effectiveness of the nanofoam electrodes at high current densities. With regards to mass transport rates during fuel cell operation, the nanofluidic fuel cell is anticipated to enhance the overall rates and reduce the mass transport overpotential compared to the microfluidic fuel cell due to the three orders of magnitude higher surface area and closer proximity of reactant flow and electrode surfaces. The measured polarization behavior at high current densities is however quite similar for the two fuel cells under investigation, which indicates that the expected mass transport benefits of the nanofluidic fuel cell are not fully realized in this case due to the high ohmic resistance of the specific nanofoam material used as electrodes. Furthermore, the crack-like macro pores observed in the SEM images (Fig. 2) may cause partial diversion of the electrolyte flow away from the active nanopores. This notion is supported by the relatively high permeability of the nanofoam compared to regular carbon paper.

The corresponding power density, calculated by multiplying current density and cell voltage, indicates that the nanofluidic fuel cell achieves approximately 6% higher peak power density than the microfluidic cell. It is noteworthy that the peak power density occurs at moderate to high current densities where the impact of ohmic losses is significant. Hence, substantially higher power densities can be anticipated with more conductive nanofoam materials. The main advantage of the nanofluidic fuel cell is however realized in the high cell voltage regime where the superior kinetic performance of the nanofluidics concept, offering 9× and 5.2× higher kinetic rate constants for V(II) oxidation and V(V) reduction, respectively, is fully exploited and less masked by ohmic losses. Here, up to 150 mV higher cell voltage and 14% higher power density are demonstrated at practical operational cell voltages as high as 1.4 V. These results are particularly important in the context of overall fuel cell efficiency, which is proportional to the operational cell voltage. Therefore, further advances in nanotechnology and in-depth studies of nanofluidics applied to fuel cell science and technology can potentially lead to a major breakthrough in regards to highly efficient and powerful fuel cell architectures.

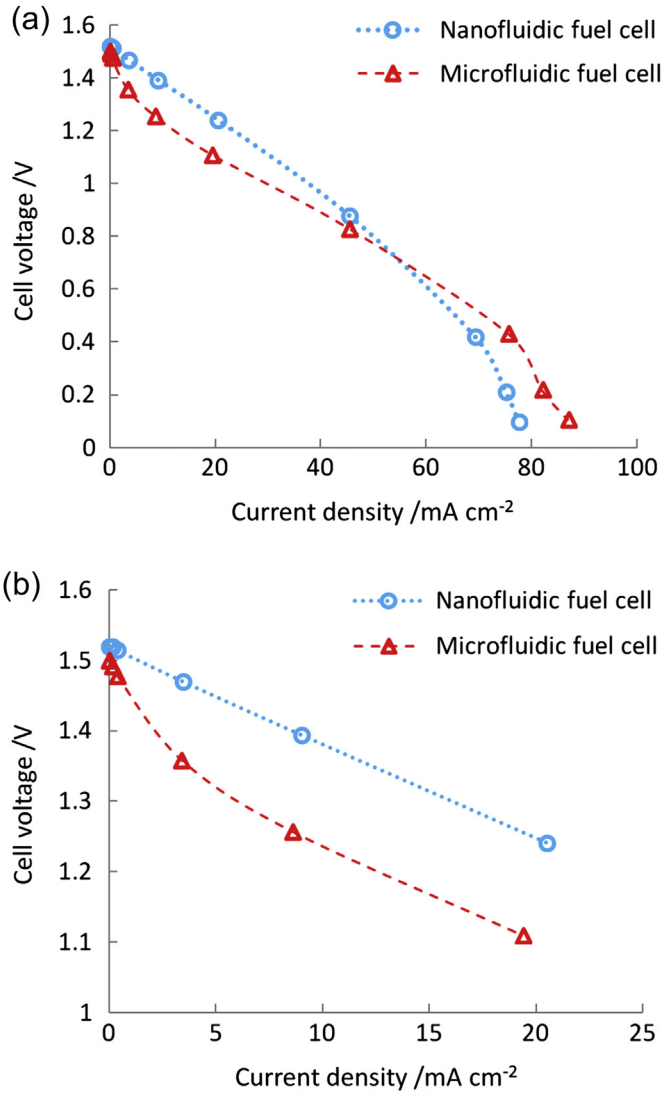

Fig. 5. Measured polarization curves for nanofluidic fuel cell operation at 10 μL min^{-1}, benchmarked against a state-of-the-art microfluidic fuel cell: (a) full polarization curve; and (b) magnified plot of the high cell voltage regime.

4. Conclusions

The present nanofluidic fuel cell demonstrates for the first time the concept of nanofluidics applied to membraneless, miniaturized fuel cells compatible with standard micromachining methods and on-chip integration. Fuel cells exploiting reactant flow through

nanoscale channels or pores inside conductive electrodes are found to exhibit (and effectively utilize) higher surface area, faster kinetics, and more well-balanced half-cells than the existing state-of-the-art microfluidic fuel cell technology, resulting in enhanced fuel cell performance. Due to the rapid electrochemical kinetics and high active surface area, nanofluidic fuel cells are found to be promising for fuel cell device operation in the high cell voltage regime where high overall fuel cell efficiency is achieved. However, as the current density is increased, high ohmic overpotentials will gradually offset the gain from its faster kinetics. Therefore, nanofoam materials with higher electrical conductivity are sought for fuel cell devices and applications that require operation at high current densities. Optimization of the electrode structure is also essential to fully exploit the rapid nanoscale transport facilitated by the nanofluidic fuel cell design. Subject to further research, this new class of fuel cell technology may potentially fill an important role in the development of low-cost, miniaturized power sources and as a future component in high-efficiency integrated clean energy systems.

Acknowledgments

Funding for this research provided by the Natural Sciences and Engineering Research Council of Canada, Western Economic Diversification Canada, Canada Foundation for Innovation, British Columbia Knowledge Development Fund, and Simon Fraser University (SFU) is highly appreciated. We also acknowledge Mr. Andy Klassen and Mr. Eugene Kizhnerman at Prudent Energy and Mr. Jun Ki Hong and Mr. Alireza Sadeghi Alavijeh at SFU for experimental assistance.

References

[1] E.R. Choban, L.J. Markoski, A. Wieckowski, P.J.A. Kenis, J. Power Sources 128 (2004) 54–60.
[2] E. Kjeang, N. Djilali, D. Sinton, Advances in microfluidic fuel cells, in: T. Zhao (Ed.), Micro Fuel Cells: Principles and Applications, Elsevier B.V., San Diego, 2009, pp. 100–137.
[3] J.W. Lee, E. Kjeang, Biomicrofluidics 4 (2010) 041301–041312.
[4] E. Kjeang, N. Djilali, D. Sinton, J. Power Sources 186 (2009) 353–369.
[5] S.A.M. Shaegh, N.T. Nguyen, S.H. Chan, Int. J. Hydrogen Energy 36 (2011) 5675–5694.
[6] A.S. Arico, P. Bruce, B. Scrosati, J.M. Tarascon, W. Van Schalkwijk, Nat. Mater. 4 (2005) 366–377.
[7] S.R. Liu, Q.S. Pu, L. Gao, C. Korzeniewski, C. Matzke, Nano Lett. 5 (2005) 1389–1393.
[8] S. Moghaddam, E. Pengwang, Y.B. Jiang, A.R. Garcia, D.J. Burnett, C.J. Brinker, R.I. Masel, M.A. Shannon, Nat. Nanotechnol. 5 (2010) 230–236.
[9] M. Tsuchiya, B.K. Lai, S. Ramanathan, Nat. Nanotechnol. 6 (2011) 282–286.
[10] A. Ziemys, M. Milosevic, M. Ferrari, M. Kojic, Interfacial effects and diffusion transport regimes in nanofluidics systems, in: Nanotechnology 2012, Nano Science and Technology Institute, 2012, pp. 705–707.
[11] D. Krishnamurthy, E.O. Johansson, J.W. Lee, E. Kjeang, J. Power Sources 196 (2011) 10019–10031.
[12] E. Kjeang, R. Michel, D.A. Harrington, N. Djilali, D. Sinton, J. Am. Chem. Soc. 130 (2008) 4000–4006.
[13] J.W. Lee, M.A. Goulet, E. Kjeang, Lab Chip 13 (2013) 2504–2507.
[14] M. Skyllas-Kazacos, G. Kazacos, G. Poon, H. Verseema, Int. J. Energy Res. 34 (2010) 182–189.
[15] J.W. Lee, E. Kjeang, Int. J. Hydrogen Energy 37 (2012) 9359–9367.
[16] W.M. Haynes, T.J. Bruno, Handbook of Chemistry and Physics, 82nd ed., CRC Press, Boca Raton, 2002.
[17] R.W. Pekala, J. Mater. Sci. 24 (1989) 3221–3227.
[18] J. Wang, L. Angnes, H. Tobias, R.A. Roesner, K.C. Hong, R.S. Glass, F.M. Kong, R.W. Pekala, Anal. Chem. 65 (1993) 2300–2303.
[19] R.W. Pekala, J.C. Farmer, C.T. Alviso, T.D. Tran, S.T. Mayer, J.M. Miller, B. Dunn, J. Non Cryst. Solids 225 (1998) 74–80.
[20] S.A. Al-Muhtaseb, J.A. Ritter, Adv. Mater. 15 (2003) 101–114.
[21] J.F. Snyder, E.L. Wong, C.W. Hubbard, J. Electrochem. Soc. 156 (2009) A215–A224.
[22] J.C. Lytle, J.M. Wallace, M.B. Sassin, A.J. Barrow, J.W. Long, J.L. Dysart, C.H. Renninger, M.P. Saunders, N.L. Brandell, D.R. Rolison, Energy Environ. Sci. 4 (2011) 1913–1925.
[23] MarkeTech. http://www.mkt-intl.com/aerogel/Carbon_Nanofoam.shtml, June 2012.
[24] I.S. Hussaini, C.Y. Wang, J. Power Sources 195 (2010) 3830–3840.
[25] J.W. Lee, J.K. Hong, E. Kjeang, Electrochim. Acta 83 (2012) 430–438.
[26] C. Fabjan, J. Garche, B. Harrer, L. Jorissen, C. Kolbeck, F. Philippi, G. Tomazic, F. Wagner, Electrochim. Acta 47 (2001) 825–831.
[27] A.A. Shah, M.J. Watt-Smith, F.C. Walsh, Electrochim. Acta 53 (2008) 8087–8100.
[28] H. Al-Fetlawi, A.A. Shah, F.C. Walsh, Electrochim. Acta 55 (2009) 78–89.
[29] E. Sum, M. Rychcik, M. Skyllaskazacos, J. Power Sources 16 (1985) 85–95.
[30] E. Sum, M. Skyllaskazacos, J. Power Sources 15 (1985) 179–190.
[31] G. Oriji, Y. Katayama, T. Miura, J. Power Sources 139 (2005) 321–324.